IVYSPRING INTERNATIONAL PUBLISHER

Theranostics

2015; 5(9): 931-945. doi: 10.7150/thno.11802

Research Paper

Smart MoS_2/Fe_3O_4 Nanotheranostic for Magnetically Targeted Photothermal Therapy Guided by Magnetic Resonance/Photoacoustic Imaging

Jie Yu[1,2,#], Wenyan Yin[2,#,✉], Xiaopeng Zheng[2], Gan Tian[2], Xiao Zhang[2], Tao Bao[2], Xinghua Dong[2], Zhongliang Wang[3], Zhanjun Gu[2,✉], Xiaoyan Ma[1,✉], Yuliang Zhao[2,✉]

1. Key Laboratory of Polymer Science and Technology, School of Science, Northwestern Polytechnical University, Xi'an, Shaanxi, China
2. CAS Key Laboratory for Biomedical Effects of Nanomaterials and Nanosafety, Institute of High Energy Physics, Beijing, China
3. School of Life Science and Technology, Xidian University, Xi'an, Shaanxi, China

[#]Jie Yu and Wenyan Yin contributed equally to this study.

✉ Corresponding authors: Wenyan Yin, CAS Key Laboratory for Biomedical Effects of Nanomaterials and Nanosafety, Institute of High Energy Physics, Beijing, China. E-mail: yinwy@ihep.ac.cn or Zhanjun Gu, CAS Key Laboratory for Biomedical Effects of Nanomaterials and Nanosafety, Institute of High Energy Physics, Beijing, China. E-mail: zjgu@ihep.ac.cn or Xiaoyan Ma, Key Laboratory of Polymer Science and Technology, School of Science, Northwestern Polytechnical University, Xi'an, Shaanxi, China. E-mail: m_xiao_yana@nwpu.edu.cn or Yuliang Zhao, CAS Key Laboratory for Biomedical Effects of Nanomaterials and Nanosafety, Institute of High Energy Physics, Beijing, China. E-mail: zhaoyuliang@ihep.ac.cn

Received: 2015.02.06; Accepted: 2015.03.20; Published: 2015.05.20

Abstract

The ability to selectively destroy cancer cells while sparing normal tissue is highly desirable during the cancer therapy. Here, magnetic targeted photothermal therapy was demonstrated by the integration of MoS_2 (MS) flakes and Fe_3O_4 (IO) nanoparticles (NPs), where MoS_2 converted near-infrared (NIR) light into heat and Fe_3O_4 NPs served as target moiety directed by external magnetic field to tumor site. The MoS_2/Fe_3O_4 composite (MSIOs) functionalized by biocompatible polyethylene glycol (PEG) were prepared by a simple two-step hydrothermal method. And the as-obtained MSIOs exhibit high stability in bio-fluids and low toxicity *in vitro* and *in vivo*. Specifically, the MSIOs can be applied as a dual-modal probe for T_2-weighted magnetic resonance (MR) and photoacoustic tomography (PAT) imaging due to their superparamagnetic property and strong NIR absorption. Furthermore, we demonstrate an effective result for magnetically targeted photothermal ablation of cancer. All these results show a great potential for localized photothermal ablation of cancer spatially/timely guided by the magnetic field and indicated the promise of the multifunctional MSIOs for applications in cancer theranostics.

Key words: Magnetic target, Photothermal therapy, Magnetic resonance imaging, Photoacoustic tomography imaging, Theranostic.

1. Introduction

There has been an increasing interest in designing nanoagents with combined diagnostic and therapeutic modalities towards personalized nanomedicine for the treatment of cancer [1-3]. Among various theranostic strategies, multimode imaging guided photothermal therapy (PTT) has gained much attention due to its lower side effects compared with the traditional chemotherapy or radiotherapy [4,5]. Near infrared (NIR) light induced PTT as a noninvasive localized cancer therapy method, can effectively convert NIR light energy into heat and finally ablate cancer cells with a high penetration depth to cancer tissue and a minimal damage to normal organs [6-8]. Up to now, various PTT nanoagents [4, 9-18] have

been investigated. However, as a typical two-dimensional (2D) graphene-like layered transitional metal MoS_2 material, only a few research groups including us have demonstrated that the MoS_2 nanoflakes had the advantage as an efficient NIR PTT nanoagent for cancer treatment due to its high NIR absorption ability [19-21]. Especially, considering its unique 2D structure with large surface area, MoS_2 nanoflakes could also be used as a nanocarrier for drug delivery [21] and a matrix material to assembly some ultra-small functional NPs to obtain multifunctional nanocomposite that exhibit better performance compared to bare MoS_2 [22-24]. Therefore, there is still a large space for us to explore the application of the MoS_2 nanoflakes.

One of the essential requirements in cancer theranostic is efficient delivery of nanotheranostic agents to the target site. Some of nanotherapeutic agents had shown effective accumulation specifically at the tumor site via passive targeting induced by the enhanced permeability and retention (EPR) effect. Moreover, tumor localization of nanostructures can be further enhanced by active targeting moiety groups on the surface of NPs [25-28]. For example, Fe_3O_4 nanoparticles (NPs), as one of the typical superparamagnetic material, have been extensively employed as a target moiety for the construction of magnetic targeting therapy systems with unique advantages i) to enable tumor specific delivery of therapeutic agents because the physical stimulus effect is more controllable and predictable under the external magnetic field; ii) to induce highly accumulation to tumor with minimal side effect to normal tissue [18, 29-31]. Therefore, integration of MoS_2 NIR photothermal ability with the strong magnetic property of Fe_3O_4 to construct a magnetic targeting PTT system could provide a unique opportunity for enhancing cancer therapy effectively. Meanwhile, Fe_3O_4, as an effective contrast agent for T_2-weighted magnetic resonance (MR) imaging, has various advantages such as high spatial resolution, noninvasive property as well as tracking the therapy effect to cancer [17, 22, 30, 32-34]. However, it cannot provide precise deep tissue signals with less real time convenience. In addition, MoS_2 could serve as a promising photoacoustic tomography (PAT) imaging contrast agent because of their highly NIR photothermal transformation efficiency, which has the ability of penetration tissues more deeply than that of other optical modalities. Multimodal imaging technique can offer synergistic advantages over any modality alone nowadays. The combination of Fe_3O_4 and MoS_2 as a dual-mode MR/PAT imaging contrast agent not only provide complementary information for enhanced tissue sensitivity but also improve tissue penetration ability. Most importantly, reports about a simple method for synthesis of the MSIOs for biomedicine application are even scarce. As a result, it is urgently needed to synthesize MoS_2 nanoflakes/Fe_3O_4 nanoparticles (MSIOs) using a simple method and explore it as a promising theranostic nanoagent for dual-modal MR/PAT imaging-guided and spatially/timely controlled magnetic targeted PTT of cancer under the external magnetic field.

Herein, a versatile theranostic nanoagent were successfully designed by a simple two-step hydrothermal method, in which ultra-small Fe_3O_4 NPs were attached on the surface of the multilayer MoS_2 nanoflakes to form MSIOs composite (Scheme 1a-b). Subsequently, the MSIOs modified by poly-(ethylene glycol) (PEG) to impart good biocompatibility were further demonstrated for magnetic targeted dual-modal MR/PAT imaging *in vitro* and *in vivo*. Moreover, the photothermal efficiency contributed by the MoS_2 nanoflakes under 808-nm NIR laser irradiation and magnetic target induced by the Fe_3O_4 in the MSIOs were utilized for realizing effective magnetic targeted photothermal ablation of cancer. Thus, the MSIOs not only have effective magnetic targeted PTT to cancer but also afford MR and PAT imaging properties (Scheme 1c). Therefore, under the external magnetic field, the MSIOs as an effective theranostic nanoagent show great potential for simultaneous multimodal MR/PAT imaging-guided diagnosis and magnetic targeting PTT to cancer.

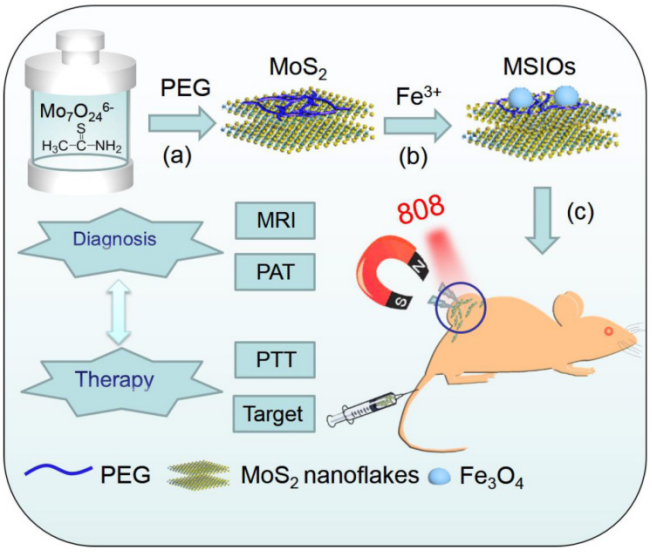

Scheme 1: Schematic illustration of the synthesis route and theranostic procedure of MSIOs for dual-modal MR and PAT imaging-guided magnetic targeting photothermal ablation of cancer.

2. Experimental Section

Materials

Ammonium molybdate tetrahydrate ($H_{24}Mo_7N_6O_{24}\cdot 4H_2O$, 99%), thioacetamide (TAA, 99%), hydrazine hydrate (50 %, v/v) and ferric trichloride anhydrous ($FeCl_3$) were purchased from Aladdin Industrial Inc. Polyethylene glycol 400 (PEG, M_w 400) and ascorbic acid (AA) were purchased from Alfa Aesar. All the chemicals were used as received without further purification. Deionized water was obtained by an 18.5 MΩ (SHRO-plus DI) system.

Synthesis of PEG modified MoS_2 nanoflakes

PEG modified MoS_2 nanoflakes were obtained by a simple hydrothermal route. Briefly, 0.5 g of PEG and 0.1766 g of $H_{24}Mo_7N_6O_{24}\cdot 4H_2O$ were sequentially dissolved in 20 mL of deionized water under stirring. After that, 10 mL of 2 mmol TAA aqueous solution was then added and stirred to form transparent solution. Then, the mixture was transferred into a Teflon-lined stainless steel autoclave and heated to 180 ^oC for 18 h. Finally, the black product was washed with ethanol and deionized water for several times by centrifugation and lyophilized for 24 h.

Synthesis of MSIOs Composite

MSIOs were synthesized by two-step hydrothermal route. In a typical process, 10 mL of $FeCl_3$ (0.0649 g) and AA (0.2113 g) aqueous solution were mixed with lyophilized PEG-MoS_2 nanoflakes (0.012 g) under ultra-sonication. Then, 6 mL of hydrazine hydrate were added. Finally, the mixture was sealed in autoclave and heated at 180 ^oC for 8 h. The precipitated MSIOs were isolated by centrifugation at 12000 rpm and washed with deionized water for 5 times. The as-obtained MSIOs were dispersed in water or cellular culture media for further use.

Cell Experiments

Hela (a human cervical carcinoma cell line) and HepG2 (a human liver hepatocellular carcinoma cell line) cells were employed for investigation the cell viability. Hela cells and HepG2 cells were grown in normal DMEM and IMDM culture medium, respectively, with 10 % fetal bovine serum (FBS). The *in vitro* cytotoxicity of these two cells were measured by a standard Cell Counting Kit-8 (CCK-8) assay. Firstly, the cells were pre-incubated in a 96-well plate (about 5000 cells/well, six wells for each concentration) for 24 h in a humidified incubator (37 ^oC, 5% CO_2). After washing each well with phosphate buffer saline (PBS, 0.01 M, pH = 7.4), the MSIOs with different concentrations (0, 6.25, 12.5, 25, 50 and 100 μg/mL) were added. Then, the cells were continuously incubated in the same condition for 24 h. CCK-8 was subsequently added to each well and the plate was kept in the incubator for another 1.5 h. Finally, the cell viability was evaluated by the absorbance at 450 nm of each well measured by a microplate reader (SpectraMax M2, MDC, USA). The cells without adding MSIOs were used as control and the cell culture medium without cells but added with CCK-8 was measured to record the background. The cell viabilities relative to the control cells were calculated.

For the photothermal ablation of cancer cell, Hela and HepG2 cells were incubated with different concentrations of PEG-MSIOs at 37 °C for 24 h. Then, an 808-nm NIR CW laser (Connet Fiber Optics Co., Ltd.) was used to irradiate the cells at a power density of 1 W/cm^2 for 10 min. After incubation for 24 h, the cells killing efficiency after the photothermal ablation were also determined by the CCK-8 assay.

Hela cells were also chosen for investigating the magnetic targeting induced photothermal ablation. Firstly, the cells were cultured for 24 h and then incubated with MSIOs with a low dosage of 10 μg/mL at 37 ^oC under 5% CO_2 with a magnet beneath the center of the culture dish. After 12 h, the magnet was removed and the cells were washed by PBS. Subsequently, the cells were washed with PBS and irradiated by the 808-nm laser for 10 min. After 12 h, the cells were washed with PBS slightly and stained with calcein AM (CA) and propidium iodide (PI) for 10 min. The redundant CA and PI were removed by PBS. Three control groups: a) cells, b) cells + NIR laser, c) cells + MSIOs + NIR laser were also stained with CA and PI. The samples were taken by the inverted fluorescence microscope (Nikon E200), and images were captured with a digital camera (Canon 450D).

Flow cytometry (FCM) analysis was carried out to determine cellular uptake. Hela Cells were used throughout the FCM analysis. The MSIOs were linked with FITC (fluorescein isothiocyanate) through a simple method. 2 mg of MSIOs dispersed in water (4 mL), were mixed with 0.1 mg FITC and stirred overnight in dark. Subsequently, FITC labeled MSIOs (FITC-MSIOs) were collected by centrifugation and washed with water and re-dispersed in DMEM media. Hela cells were seeded in 6-well plate and incubated at 37 ^oC under 5% CO_2 for 24 h. After washed with PBS, the cells were incubated with FITC-MSIOs dispersion for 2 h with final MSIOs concentration of 10 μg/mL. Finally, the cells were washed by PBS, and suspend in PBS for FCM analysis (Accuri c6, DB, USA).

In vitro Dual-modal MR and PAT Imaging

T_2-weighted MR imaging *in vitro* of MSIOs with different concentrations (0, 0.0125, 0.025, 0.05, 0.10,

0.20 mg/mL) of Fe_3O_4 in the MSIOs dispersed in 0.5% agarose gel which was filled in the NMR tube were scanned using a 4.7 T MR imaging instrument (Biospec; Bruker, Ettlingen, Germany) at the room temperature. The signal intensity was recorded using a region-of-interest (ROI) for each sample after acquiring the MR images. Also, the relaxation rates r_2 ($r_2 = 1/T_2$) were calculated from the T_2 values at different of Fe_3O_4 concentrations in the MSIOs. For the PAT imaging of MSIOs *in vitro*, 1 mL of the MSIOs aqueous solution with various concentrations (0, 0.025, 0.05, 0.1, 0.2, 0.5, 1.0 mg/mL), was added into the agarose phantom container and installed in the multispectral optoacoustic tomography (MSOT) system (COLD SPRING BIOTECH CORP. inVision 128) for the signal acquisition. The PAT imaging signals of the MSIOs were collected under an irradiation range from 680 to 900 nm.

Animal Model, *in Vivo* MR and PAT Imaging

BALB/c nude mice (18 g in weight, male) were purchased from Cancer Institute & Hospital, Chinese Academy of Medical Sciences, and used under protocols approved by the Institute's Animal Care and Use Committee. For the pancreatic tumor (PANC-1) model, 1 x 10^7 PANC-1 cells in ≈ 100 μL of serum-free DMEM medium were subcutaneously injected onto the backside of each mouse. The mice were used when the tumor volumes approached ~100 mm^3.

For the MR and PAT imaging, the magnet was placed on the tumor area of each mouse by using medical adhesive tape. After that, the MSIOs (200 μL, 1.0 mg/mL) in PBS were intravenously (*i.v.*) injected into the tail vein of the tumor-bearing mice. The mice were then anaesthetized by pentobarbital sodium (1%, PBS solution) at a dosage of 40 mg/kg body weight. *In vivo* MR imaging was performed with a 1.5 T clinical MRI system equipped with a special coil (SIEMENS Syngo) before injection and 0.5, 6, and 24 h post injection of the mice, respectively. Whereas for *in vivo* PAT imaging, the mice *i.v.* injected with the same dose of MSIOs as the MR imaging were imaged before injection (0 h) and 0.5, 6 h post injection by using the COLD SPRING BIOTECH CORP. MSOT inVision 128 system. The obtained PAT imaging signal is range from 680-900 nm as the excitation laser and the ROI is 20 mm. After finishing the experiment, the mice were disposed according to the standard protocol approved by the Key Laboratory for Biomedical Effects of Nanomaterials and Nanosafety (Institute of High Energy Physics, CAS).

In vivo Biodistribution and Pathology Analysis of MSIOs

Inductively coupled plasma mass spectrometry (ICP-MS) were used for the determination the biodistribution of the MSIOs in BALB/C tumor-bearing mice (male, 7 weeks years old). The mice were *i.v.* injection with the MSIOs of 20 mg/kg body weight. At the proper time intervals, the mice were sacrificed. The organs were dissected, weighted and put into flask. Then, 5 mL of HNO_3 was added to each flask. The flasks were placed onto a hot plate and maintained at 150 ^oC until all the organs were digested. After cooling to room temperature, the solution was diluted to 4 mL with 2 % HNO_3. Before the ICP-MS analysis, the Mo standard solutions with different concentrations of 0, 0.5, 1, 5, 10, 50, and 100 ppb were prepared with the 2 % HNO_3 solution. Both the standard solutions and the organs solutions were measured by ICP-MS. The amount of MSIOs was finally normalized to the tissue weight per gram. The mice without injection of MSIOs were acted as control groups.

The long-term toxicity within 15 days of the MSIOs *in vivo* was evaluated by the body weight of tumor-bearing mice. To further identify the biocompatibility, the major organs of the mice before and post injection at the 7-day were collected, respectively, fixed in 10% neutral buffered formalin, processed routinely into paraffin, stained with hematoxylin and eosin (H&E). The pathology slices were examined by a digital microscope. The tissues including heart, liver, spleen, kidney, and lung were examined.

Magnetic targeting induced therapeutical evaluation of MSIOs for tumor bearing mice

Tumor bearing BALB/C nude mice were also prepared by inoculating 1x10^7 PANC-1 cells through subcutaneous injection. When the tumor size reached approximately 100 mm^3, the mice were divided into four groups: (I) PBS injection; (II) laser only; (III) MSIOs (*i.v.* injection) + laser; and (IV) MSIOs (*i.v.* injection) + magnet + laser. Then, the PANC-1 tumor bearing mice were injected with MSIOs (a low dosage of 100 μL, 1.0 mg/mL) when the MSIOs were injected after 24 h (III and IV). And then, the tumors were exposed to 808 nm laser (power density: 1 W cm^{-2}, 12 min). NIR thermal images and the temperature change at the tumor sites were recorded by a NIR imager (E40, FLIR) for II, III, and IV groups. Photos were acquired at different time points to observe the thermal imaging effects in the treatment group. The tumor sizes were measured by a caliper every other day. The tumor volumes and the tumor weights were also calculated during the experiments. Then, the mice were sacrificed at the 15-day, the tumors were dissected and weighed to evaluate the therapeutic efficacy.

Characterization of MSIOs

The size and morphology of the products were determined with a field emission scanning electron microscopy (FE-SEM, Hitachi High Technologies, Japan) and a TecnaiG2 F20 U-TWIN transmission electron microscope (TEM) and scanning transmission electron microscopy (STEM) operated at 200 kV. The elements distributions of the samples were examined by the TEM equipped with an energy-dispersive X-ray spectrum (EDX, HORIBA EMAX-250). Atomic force microscopy (AFM) images of the MoS_2 nanoflakes were captured by a Multi-Mode V AFM (Agilent 5500, Agilent, USA). Their thickness were measured based on sheet heights in AFM images. Dynamic light scatting (DLS) and zeta potential (ζ) analysis were performed on a Nicomp380 ZLS plus ZETADi. X-ray powder diffraction (XRD) analyses were performed using a Japan Rigaku D/max-2500 X-ray powder diffractometer with Cu K_a radiation (λ = 1.54 Å). Raman spectra were recorded by a Raman spectrometer (Horiba LabRam HR 800). Ultraviolet-Visible-Near Infrared spectroscopy (UV-Vis-NIR, Cary 5000, Agilent, USA) were used for the absorbance measurements. The photothermal effects of MSIOs were measured by an infrared thermal imager (E40, FLIR) and the temperature changes were recorded one time per 20 s when an 808 nm NIR laser was oriented perpendicular to a quartz cuvette containing the as-detected MSIOs dispersions with various concentrations (total volume: 1 mL). The content of Mo element in MSIOs was measured by ICP-MS (Thermo Elemental X7, USA). The X-ray photoelectron spectroscopy (XPS) measurements were carried out with an ESCALab220i-XL spectrometer using a twin-anode Al K_a (1486.6eV) X-ray source. All the spectra were calibrated to the binding energy of the adventitious C1s peak at 284.6 eV.

3. Result and Discussion

Characterization of MSIOs

MSIOs were prepared by a simple two-step hydrothermal strategy as depicted in Scheme 1. In this structure, the MoS_2 nanoflakes was mainly responsible for exerting photothermal agent and PAT imaging contrast agent owing to its high NIR absorption ability while Fe_3O_4 was employed as magnetic targeting and MR imaging contrast agent to construct the dual-modal imaging-guided targeting PTT to cancer. PEG was used to modify the MoS_2 to prevent aggregations of the nanoflakes and improve the water-solubility as well as the biocompatibility. A TEM image in Figure 1a reveals that the as-obtained MoS_2 nanoflakes exhibit multilayer flake structure with an ultimate average size of 100 nm during the first hydrothermal step. The high-resolution TEM (HRTEM) image in Figure 1b indicates the crystal lattice fringes with *d*-spacing of 0.275 nm can be assigned to the (100) plane of hexagonal MoS_2, which is consistent with the 2H-MoS_2 (PDF card No. 37-1492) [35]. AFM image illustrates the thickness of the nanoflakes is 8-12 nm with a curved surface (Supplementary Figure S1). For preparing the MSIOs, the second step hydrothermal synthesis is used. As can be seen from the Figure 1c-d, Fe_3O_4 NPs with the diameter of ~5 nm adhered to the surface of MoS_2 nanoflakes, suggesting a strong interaction between the NPs and nanoflakes. Dynamic light scatting (DLS) analysis revealed that the MSIOs have narrow size distributions with the average hydrodynamic size of 190.1 nm (Supplementary Figure S2). The ζ potential value of MSIOs is -21.9 mV approximately, which is lower than that of the pure MoS_2 nanoflakes (-23.1 mV). The HRTEM image shows the crystal lattice fringes with *d*-spacing of 0.297 nm can be assigned to the (220) plane of the Fe_3O_4, which is agreement with the cubic phase Fe_3O_4 (PDF card No. 85-1436) [36]. In addition, the FE-SEM images indicate that the amount of Fe_3O_4 NPs on MoS_2 nanoflakes can be effectively tuned by the initial addition of Fe^{3+} ions (Supplementary Figure S3). Figure 1e shows XRD patterns of as-synthesized MoS_2 nanoflakes (red line) and MSIOs (dark line), respectively. Typical 2H-MoS_2 crystal diffraction pattern can be indexed as the hexagonal phase of MoS_2 (JCPDF No. 37-1492) during the first hydrothermal process. After the second step hydrothermal route, another five diffraction peaks can be directly indexed as the cubic phase of Fe_3O_4 (JCPDF No. 85-1436), indicating the good stability of MoS_2 nanoflakes and the successful attachment of Fe_3O_4 to the MoS_2 flakes to form MSIOs by using two-step hydrothermal method. Raman spectrum can further confirm the MoS_2 phase structure (Figure 1f). The Raman spectrum of the bulk MoS_2 sample shows the bands at 381 and 406 cm^{-1}, which correspond to the E^1_{2g} and A_{1g} modes, respectively. Significantly, the E^1_{2g} and A_{1g} modes in both MoS_2 nanoflakes and MSIOs are clearly soften and broaden compared with the bulk sample, indicating that the lateral dimensions of these layers are in the nanoregime and a phonon confinement present in these samples [37]. Also, the obvious red-shifts of the Raman peaks for the MoS_2 nanoflakes and MSIOs further implied that they have a multilayer structure [38].

The MSIOs composite was confirmed by the EDX spectra (Supplementary Figure S4) and element mapping. As shown in Figure 2a-b, the element mapping indicates the presence of Fe and O elements signals around the Mo and S signals, further indicating that the Fe_3O_4 NPs are located on the surface of

MoS_2 nanoflakes. XPS analysis gives more detailed chemical state of the MoS_2 (Supplementary Figure S5) and MSIOs (Figure 2c-g). Figure 2c shows a survey XPS plot of the MSIOs with peaks of Mo, S, Fe, and O elements. In Figure 2d, three XPS peaks at 228, 232 and 235 eV correspond to the $Mo3d_{5/2}$ (Mo^{4+}), $Mo3d_{3/2}$ (Mo^{4+}), and $Mo3d_{5/2}$ (Mo^{6+}), respectively, and the lower-energy peak at ~225 eV represents the S2s orbital signal. The XPS curve of S2p elements are shown in Figure 2e, two peaks at 161 and 162 eV, correspond to the $2p_{3/2}$ and $2p_{1/2}$ of divalent sulfide ions (S^{2-}), and a peak at 168 eV correspond to the $2p_{3/2}$ of hexavalent sulfide atom in sulfate (SO_4^{2-}), respectively. The slight change of the oxidation state of Mo and S elements could be attributed to the negligible surface oxidation of MoS_2 nanoflakes during second hydrothermal step and the relative elements atom content analysis implied the absorption of Fe containing compound on the MoS_2 nanoflakes surface (Supplementary Table S1). All these results further prove that the as-prepared MSIOs sample consist of MoS_2, which is in good agreement with those reported values of MoS_2 crystal although a negligible oxidation of Mo^{4+} to Mo^{6+} was found due to the hydrothermal process [39]. The XPS curve of Fe2p with a peak at 710 eV can be observed in Figure 2f. The two fitted curves with the peaks at 708.8 and 709.7 eV reveal that a new compound composed of Fe and S elements are formed on the surface of MSIOs, which is composed of ferric and ferrous iron and divalent sulfur in MSIOs, respectively [40], suggesting the existence of Fe-S bond. The XPS curve of Fe2p with peaks at 711.3, 712.4, and 713.6 eV can be assigned to the Fe^{3+} and peaks at 709.3 and 710.4 eV can be assigned to the Fe^{2+} in Figure 2f, which are the characteristic peaks of $Fe2p_{3/2}$ in Fe_3O_4, suggesting the coexistence of Fe^{2+} and Fe^{3+} [41]. Figure 2g shows O1s curve with peaks at 529 and 531 eV, respectively. The peaks at 529 eV can be attributed to the lattice oxygen of Fe_3O_4 and the 531 eV can be assigned to the hydroxyl group originating from the surface modification [42].

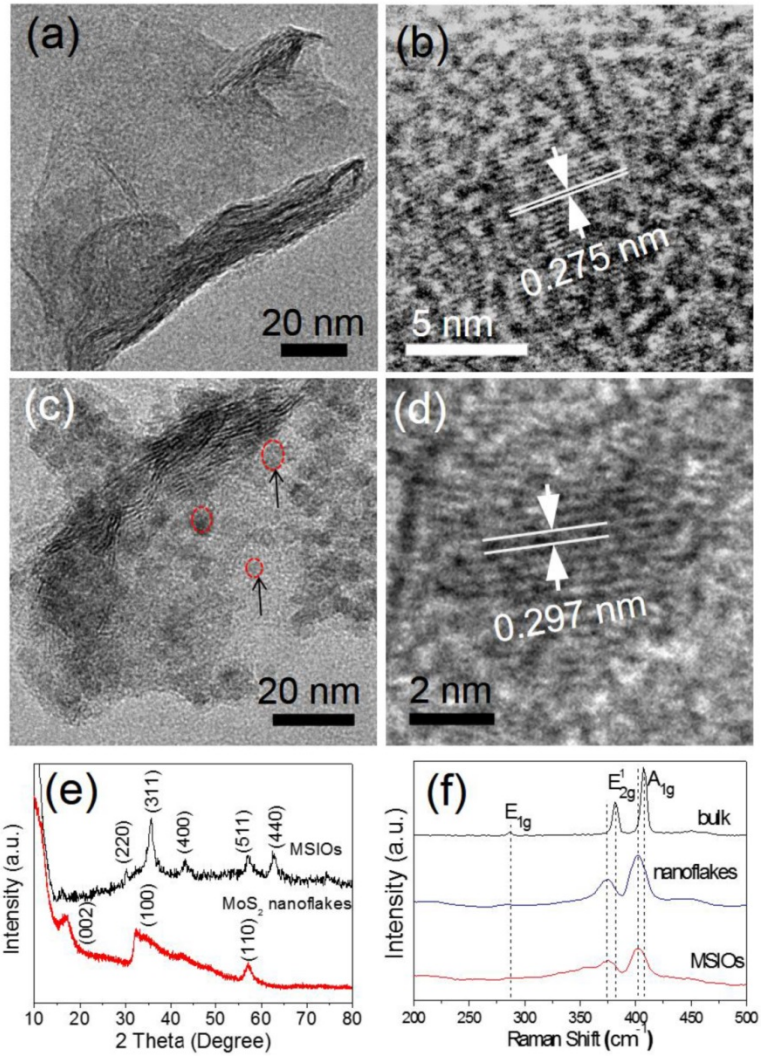

Figure 1. TEM images of (a-b) MoS_2 and (c-d) MSIOs, respectively. (e) XRD patterns of MoS_2 and MSIOs. (f) Raman spectra of bulk MoS_2, multilayer MoS_2 and MSIOs nanoflakes.

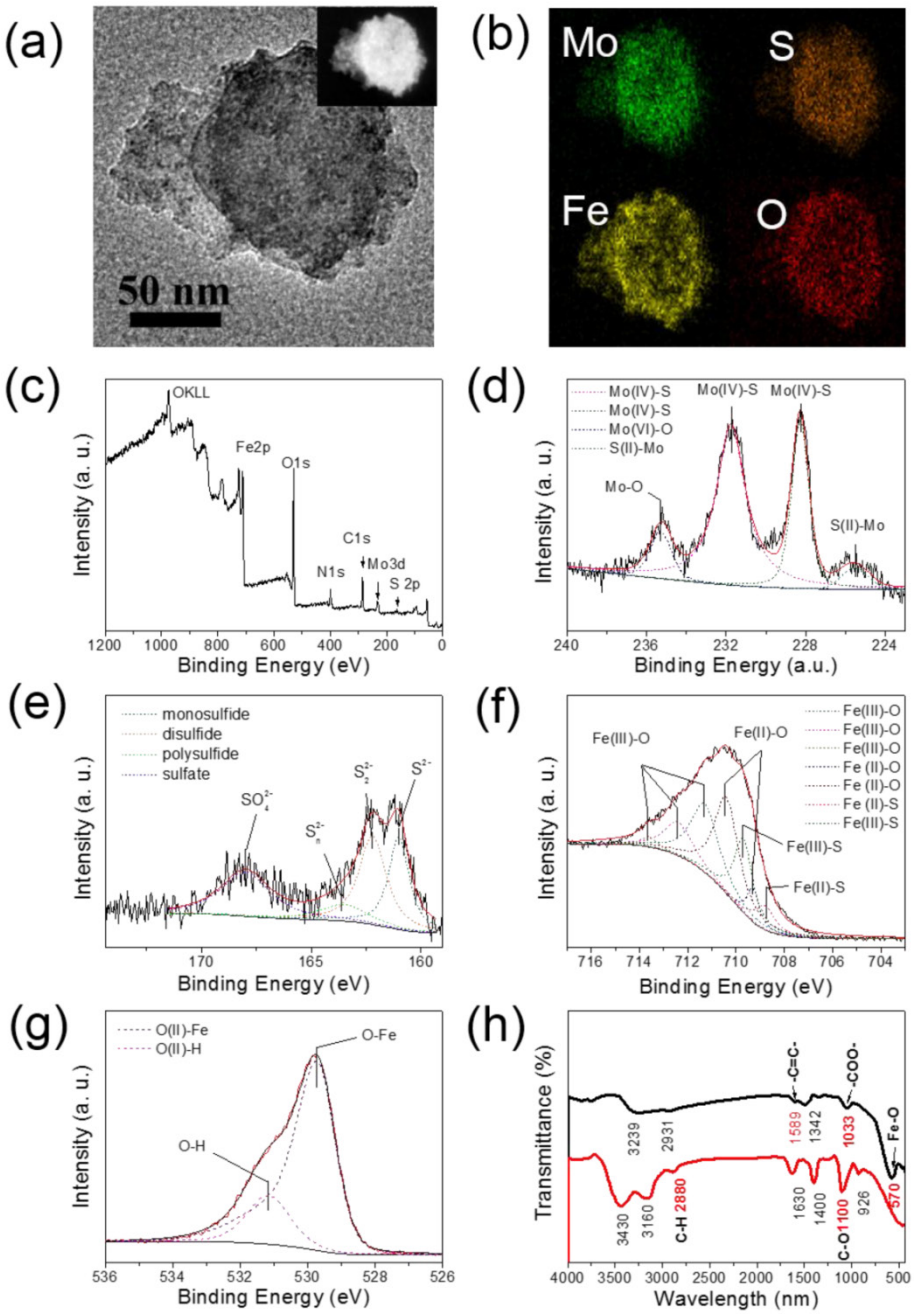

Figure 2. (a) TEM and (b) corresponding EDX element mapping images of MSIOs, revealing the distribution of Mo(Green), S(sienna), Fe(yellow) and O(red) elements. (c) XPS survey spectrum of MSIOs and (d) Mo, (e) S, (f) Fe, and (g) O elements XPS spectra, together with their corresponding fitting curves (the fitting curves were marked with the dotted lines). (h) FT-IR spectra of MSIOs (Red line: MoS_2 nanoflakes, black line: MSIOs). Inset in (a): STEM image of the MSIOs.

Moreover, for safe application in biomedical field, the MSIOs were modified by PEG. The surface function group of the MoS_2 and MSIOs were characterized by FT-IR spectra as shown in Figure 2h. The curve of MoS_2 nanoflakes with typical peaks at 1100, 1630, and 2880 cm^{-1} are attribute to C-O-C, C-O and C-H bond vibration in PEG [43], revealing that PEG was successfully modified on the surface of MoS_2. For the MSIOs, the Fe-O bond peak of the Fe_3O_4 NPs is observed at 570 cm^{-1} [44]. In addition, two typical peaks at 1589 and 1033 cm^{-1} are attributed to the alkene double bond and OH bond vibrations in carboxyl group [45], illustrating that the AA was also located on the surface of the MSIOs.

To ensure the successful formation of Fe_3O_4/MoS_2 nanocomposites, the loading amount of Fe_3O_4 should be well controlled by varying the concentration of Fe precursor. For example, when the ratio between Fe precursor and MoS_2 is lower than 5:1, our result showed that most Fe_3O_4 NPs are attached on the surface of MoS_2. On the contrary, more Fe precursors added into the reaction system will

cause the separation of Fe_3O_4 nanoparticles from the MoS_2 nanoflakes since there are no extra sites on the surface of MoS_2 for the absorption of Fe^{3+} ions. The anchoring strength between Fe_3O_4 NPs and MoS_2 nanoflakes could be explained as follows: (i) MoS_2 with large specific surface area can provide an interface for absorption the Fe_3O_4 NPs; (ii) MoS_2 nanoflakes have a negative charge surface according to the ζ potential measurements results (-23.1 mV), they could be further easily anchored with the positively charged Fe^{3+} through electrostatic interaction, and then, Fe_3O_4 NPs were formed on the MoS_2 surface under the existence of reducing agent.

In Figure 3a, it can be clearly seen that the PEG modified MSIOs have a good stability in biological media including DMEM, FBS, PBS, as well as water for at least 2 days, allowing the MSIOs to be further used in biological or physiological environments. Magnetization measurements showed that MSIOs possess a saturation magnetization of 33.4 emu/g, indicating a super-paramagnetic nature of the MSIOs at room temperature (Figure 3b). The UV-Vis-NIR absorbance spectrum of MSIOs exhibits a strong absorption band from UV to NIR region (Supplementary Figure S7), which has a negligible decrease for the absorption at the 808 nm compared with the pure MoS_2 with the same content as the MSIOs. To verify the potential use of MSIOs as a PTT agent, the MSIOs aqueous solutions with different MoS_2 concentrations were irradiated with 808-nm NIR laser at a power density of 1 W cm^{-2} for 10 min. In marked contrast to the water sample, the MSIOs solution shows a concentration-dependent temperature increase (Figure 3c,d). The NIR photothermal transduction ability of MSIOs was also investigated when the temperature change of the MoS_2 nanoflakes with concentration of 170 ppm as a function of time were measured under the 808 nm laser (1.0 W/cm^2, 10 min) (Supplementary Figure S8). According to the obtained data, the photothermal conversion efficiency of MSIOs can reach ~43.93% (Supplementary Material).

In vitro dark cytotoxicity and magnetic targeting photothermal induced PTT of Cancer

To study the dark cytotoxicity of PEG modified MSIOs without laser irradiation, the standard cell viability Cell Counting Kit-8 (CCk-8) assay was investigated to determine the viabilities of Hela and HepG2 cells after being incubated with various concentrations of MSIOs for 24 h. It was found that no obvious toxicity could be observed for the two cells and cell viabilities can remain above 80% even at high concentrations up to 200 μg/mL (Figure 4a-b). As shown in Figure 4a (the black bars), for the Hela cells, more than 82 % of cell viability was observed at the concentration of 200 μg/mL after incubation with the MSIOs. And the cell viability of the HepG2 cells was greater than 85 % at the concentration of 200 μg/mL (Figure 4b, the black bars). In addition, the cellular uptake of the as-prepared MoS_2 and MSIOs for Hela cells were conducted by the flow cytometry, respectively. The results exhibited in Supplementary Figure S9 confirm a well affinity between cells and the samples.

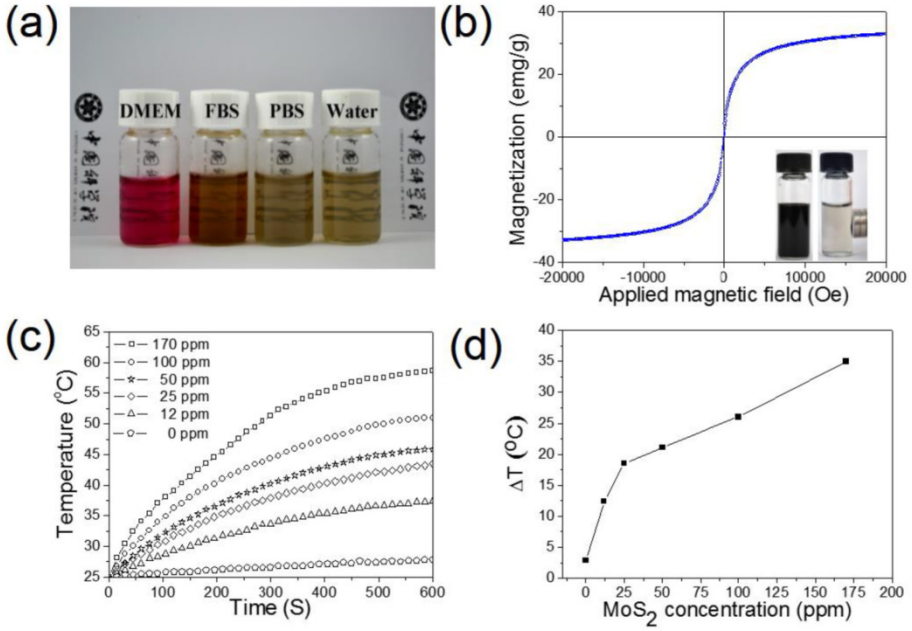

Figure 3. (a) Stability tests of MSIOs in DMEM, FBS, PBS, and water dispersions. (b) Magnetization loops of MSIOs. Inset is a photo of MSIOs solution placed nearby magnets. (c) Temperature changes based on the MoS_2 concentration in the MSIOs dispersion under 808-nm NIR laser irradiation (the stoichiometric composition of the MoS_2 was quantified by the ICP-MS based on Mo element). (d) Temperature change plot over the time of 10 min *versus* different MoS_2 concentration in the MSIOs dispersion in (c).

Subsequently, the MSIOs were applied for photothermal ablation of cancer cells under the NIR 808 nm laser irradiation. As shown in Figure 4 (the red bars), the MSIOs with various concentrations were incubated with Hela or HepG2 cells for 24 h and then irradiated by the 808 nm laser (1.0 W/cm^2) for 10 min. The relative viabilities of cells decreased as the concentration of MSIOs increased. The cytotoxic effects after NIR 808 nm irradiation indicated that about 5.3 % of Hela and 28 % of HepG2 cells were killed by MSIOs at the concentration of 200 μg/mL. In contrast, the cells without laser irradiation were not affected after the same incubation condition. These results demonstrate that MSIOs could be acted as a potent nanoagent for photothermal ablation of cancer cells.

Due to the strong magnetism of MSIOs, they have the potential and advantage for magnetic targeting photothermal therapy of cancer. Therefore, in our experiment, Hela cells were incubated with a low dose of 10 μg/mL of MSIOs for 12 h in the external magnetic field as shown in Figure 5a-b. The cells without/with NIR laser and the cells incubated with the MSIOs (10 μg/mL) without magnetic targeting under NIR 808 nm laser irradiation were acted as control groups (Figure 5c-e). All the cells were stained with CA and PI to differentiate live (green) and dead (red) cells, respectively. As shown in Figure 5a-b, a gray circle appeared in the center of culture dish, indicating the accumulation of MSIOs around the magnet. Then, the dish were irradiated by the 808 nm laser for 10 min and further cultured for another 12 h in the location of the circle (Figure 5f-i). It can be observed that a large number of cells near the magnet were destroyed (Figure 5f-h), while those in the magnet were almost completely destroyed by the photothermal ablation (Figure 5i) compared with the control groups. The remarkable magnetic targeted enhanced photothermal ablation property of the low dose MSIOs to cancer cells *in vitro* predicts their possibility as an effective magnetic response PTT nanoagent *in vivo*.

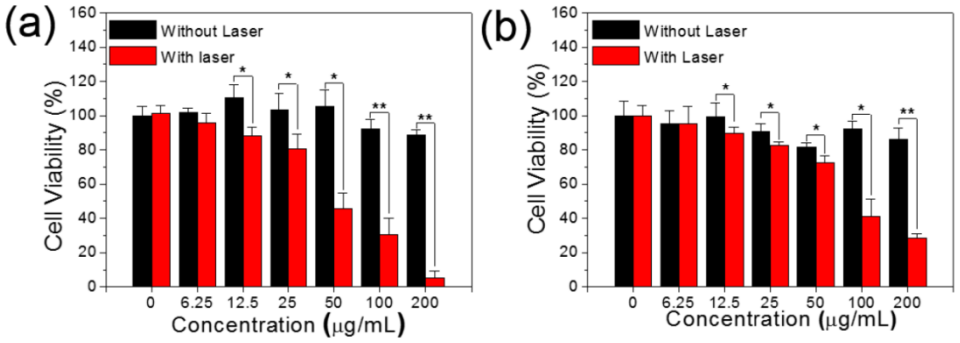

Figure 4. The black bars: Dark cytotoxicity of (a) Hela and (b) HepG2 cells treated by different concentrations of MSIOs for 24 h without laser irradiation, respectively.. The red bars: Photothermal induced cytotoxicity of (a) Hela and (b) HepG2 cells treated by different concentrations of MSIOs with the 808 nm laser irradiation (1 W/cm^2, 10 min), respectively. *P < 0.05; **P < 0.01.

In vivo cytotoxicity of MSIOs

For the further use of MSIOs as a magnetic targeting PTT agent *in vivo*, it is necessary to understand the potential toxicology of the MSIOs. Therefore, the *in vivo* toxicity assessments of the MSIOs including the histological sliced analysis, biodistribution and body weight, were conducted. BALB/C tumor-bearing mice were *i.v.* injected with a dose of MSIOs of 20 mg/kg of body weight (200 μL, 2 mg/mL). Compared with the control group, the histological examination of hematoxylin and eosin (H&E) stained slices of the major organs such as heart, liver, spleen, lung and kidney showed that there were no noticeable organ damage and inflammatory lesion for all the major organs of the mice after injection with MSIOs for 7 days (Figure 6a). Also, no necrosis was found in any of the groups. The biodistribution results in Figure 6b detected by ICP-MS indicated that the early high concentration accumulation of MSIOs in the liver and spleen was expected which was related to the clearance of foreign materials by the macrophage system within 24 h [34]. At the 48 h time point, there was a slight decrease in the amount of the MSIOs in the liver and spleen, suggesting the gradually clearance from the two organs. After 7 day, notable decreases of the MSIOs in the liver and spleen were found, indicating that the MSIOs have an overt clearance from the two organs. Also, a relatively high accumulation of the MSIOs within tumor can be observed within 24 h and gradually clearance from the tumor at the 48 h and 7 day. A combined effect of a locally increased capillary permeability at the tumor site due to the EPR effect and the strong magnetic targeting effect may be responsible for the increased accumulation of MSIOs within 24 h, which was proved by the ICP-MS result (Supplementary Figure S10). Meanwhile, fluctuation of body weight is a useful indicator for investigating the toxicity effect of the MSIOs. No significant body weight loss was observed in the treated group over a period of 15 days (Figure 6c). These results proved that MSIOs at the given dose hardly cause *in vivo* toxicity and could be used as an injectable theranostic agent *in vivo*.

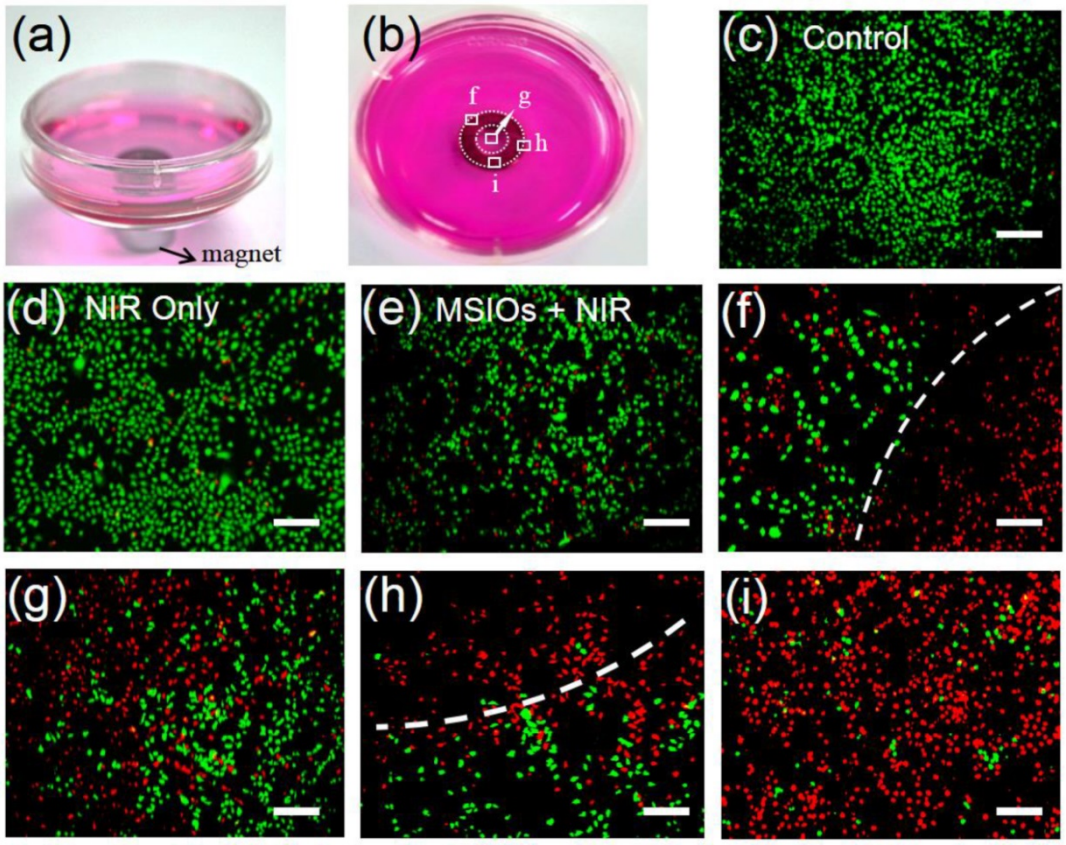

Figure 5. Photographs of magnetic targeting induced cells ablation under 808 nm laser irradiation in culture plate with a donut shaped magnet beneath (marked by donut circles). (c-i) Fluorescence images of CA and PI co-staining of Hela cells without (c-d) and with (e-i) incubation of MSIOs before and after exposure to NIR 808-nm laser. (e) Cells treated with MSIOs and 808 nm laser but without magnetic fields. (f-i) Magnetic targeting induced photothermal ablation to cancer cells corresponding to square box area from (f) to (i) in photo (b). Dash lines depict the boundaries of dead cells (red) and living cells (green) region. (Scale bar: 100 μm)

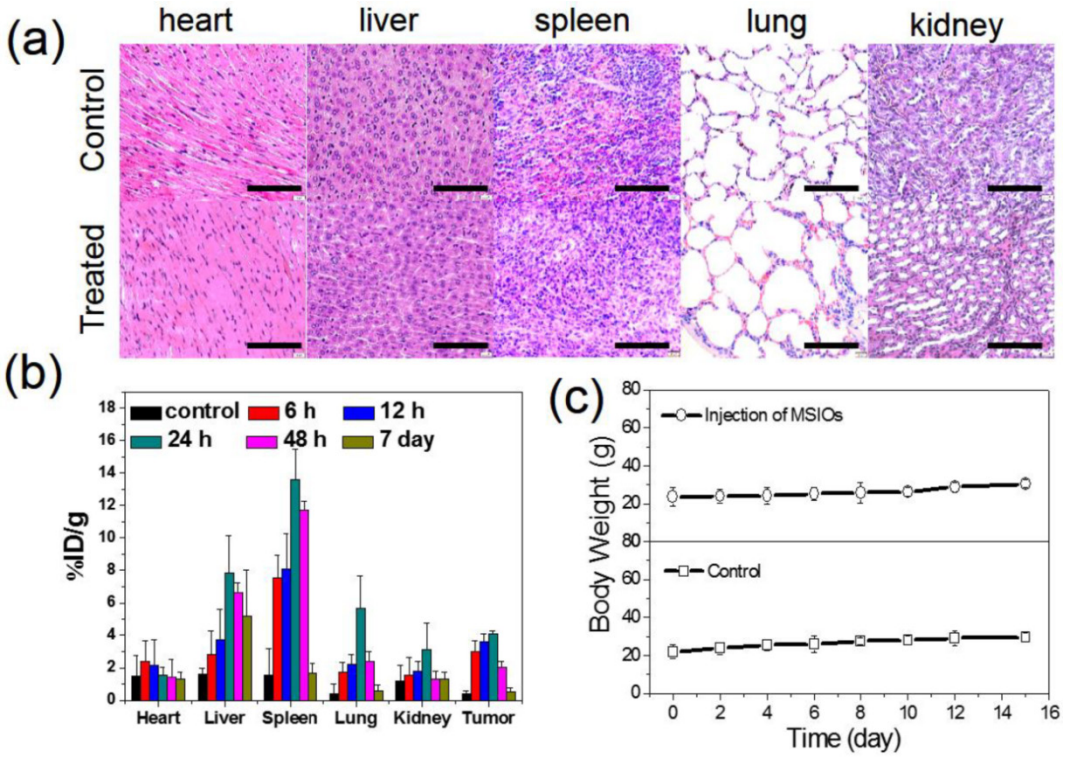

Figure 6. (a) H&E-stained histological slices from mice receiving no injection (control) and (b) post-injected with the MSIOs for 7 day. (b) Biodistribution of the MSIOs in different time intervals after injection of MSIOs determined by ICP-MS measurements of Mo element in tissue lysates. (c) Body weights change of the post-injected mice within 15 day compared with the control group without injection of MSIOs. Scale bars in (a) is 100 μm.

Dual-modal MR/PAT imaging *in vitro* and *in vivo*

Multimodality biomedical imaging technique plays a key role in medical diagnostic field, which can combine advantages of each method alone, thus became one of the research hotspots in recent years. Due to its high resolution and noninvasive property, T_2-weighted MR imaging is one of the powerful techniques in cancer diagnosis, which has been investigated by many groups focusing on several kinds of contrast agent [46,47]. Also, magnetic Fe_3O_4 NPs have been widely used as a contrast agent for MR imaging. In our experiment, the MSIOs aqueous solutions with different Fe_3O_4 concentrations were investigated by T_2-weighted MRI scanner to assess their contrast enhancement effect *in vitro*. In Figure 7a, the T_2 signal intensity significantly decreased and the image darkened with the increase of the Fe_3O_4 concentration of the MSIOs which can be attributed to the dipolar interaction of the magnetic moments with protons in the water. The MSIOs with a series of concentrations were also employed to investigate the r_2 value, which is calculated from a fitting curve of the longitudinal relaxation rate ($1/T_2$, r_2) as a function of the Fe_3O_4 concentration. The r_2 value is calculated to be 203.69 $mg^{-1}\ s^{-1}$. The good performance in MR imaging of the MSIOs demonstrates that they are promising candidate as T_2-weighted MR imaging contrast agent. Moreover, PAT imaging has been paid more and more attention due to the advantages of enhancing the penetration depth by using NIR light [17]. The MSIOs could be used as PAT imaging contrast agent due to the strong NIR absorption and photothermal transduction ability of MoS_2. Similar with the MR imaging experiment, varied concentrations of MSIOs water solution in phantom gels containers were used to obtain the PAT images. As shown in Figure 7b, with the increase of the MSIOs concentration, the enhancement of PAT signal and linearly dependent on the concentration of the MoS_2 in the composite (r^2 = 0.995) are clearly observed, suggesting the high PAT contrast potential of MSIOs. MR and PAT imaging results proved that MSIOs have a promising application as a dual-modal theranostic nanoagent.

Next, T_2-weighted MR imaging *in vivo* were performed at several time points (0 h (pre-injection), 0.5 h, 6 h, and 24 h) after administration with MSIOs (200 μL, 1 mg mL^{-1}). The anaesthetized mouse was acted as the control for MR imaging. After that, the magnet was adhered on the tumor site of the mice for 2 h after *i.v.* injection. Then, the magnet was removed before MR imaging. As shown in Figure 8a, the obviously darkened T_2 signal, indicated the enhanced MR imaging effectiveness in tumor site with the prolonged injection time. The MR image in the time point of 24 h reached the most obvious compared with the other time point. In addition, the PAT imaging *in vivo* was investigated. The tumor bearing mice were *i.v.* injected by using the MSIOs with a magnetic conglutination on the tumor before imaging, and the PAT imaging signals of tumor were recorded at different time intervals (Figure 8b). Before *i.v.* injection, the image showed observable but weak PAT signals in the tumor region, arising from the contrast of tumor's blood. After *i.v.* injection for 0.5 and 6 h, the contrasts in the tumor site remarkably enhanced, indicating the gradual homing of MSIOs into tumors with the time increase. However, the PAT imaging without magnetic field showed a relatively low accumulation in tumor compared with the magnetic targeting induced PAT imaging (Figure 8c). The result clearly indicated that the MSIOs have satisfactory residence time in tumor and efficient magnetic targeting to tumor site. Both the use of PEG modified MSIOs which may favor the efficient EPR effect and the magnetic positive targeting of Fe_3O_4 under external magnetic field in tumor could explain the effective PAT imaging result.

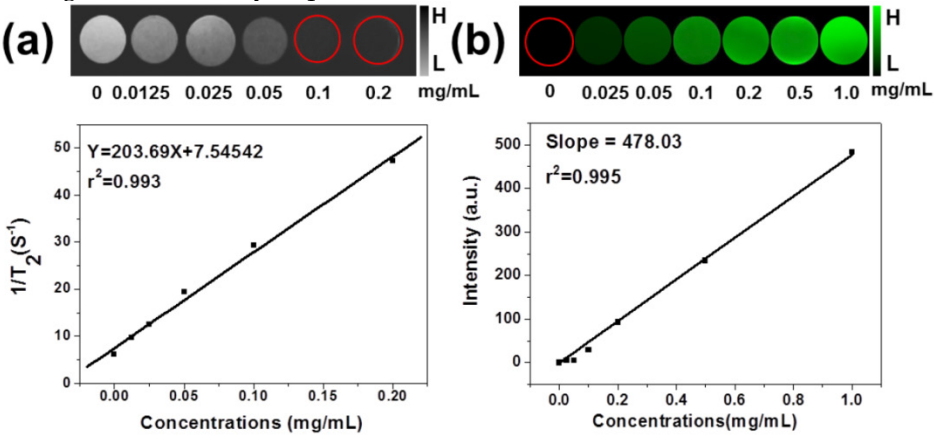

Figure 7. (a) *In vitro* T_2-weighted MR images with different concentrations of Fe_3O_4 in MSIOs and T_2 relaxation rates $1/T_2$ (r_2) plot of different concentrations of Fe_3O_4 in MSIOs. (b) *In vitro* PAT images of MSIOs with different concentrations in a phantom gel container and plot of photoacoustic signal *versus* a series of concentrations of MoS_2 in MSIOs.

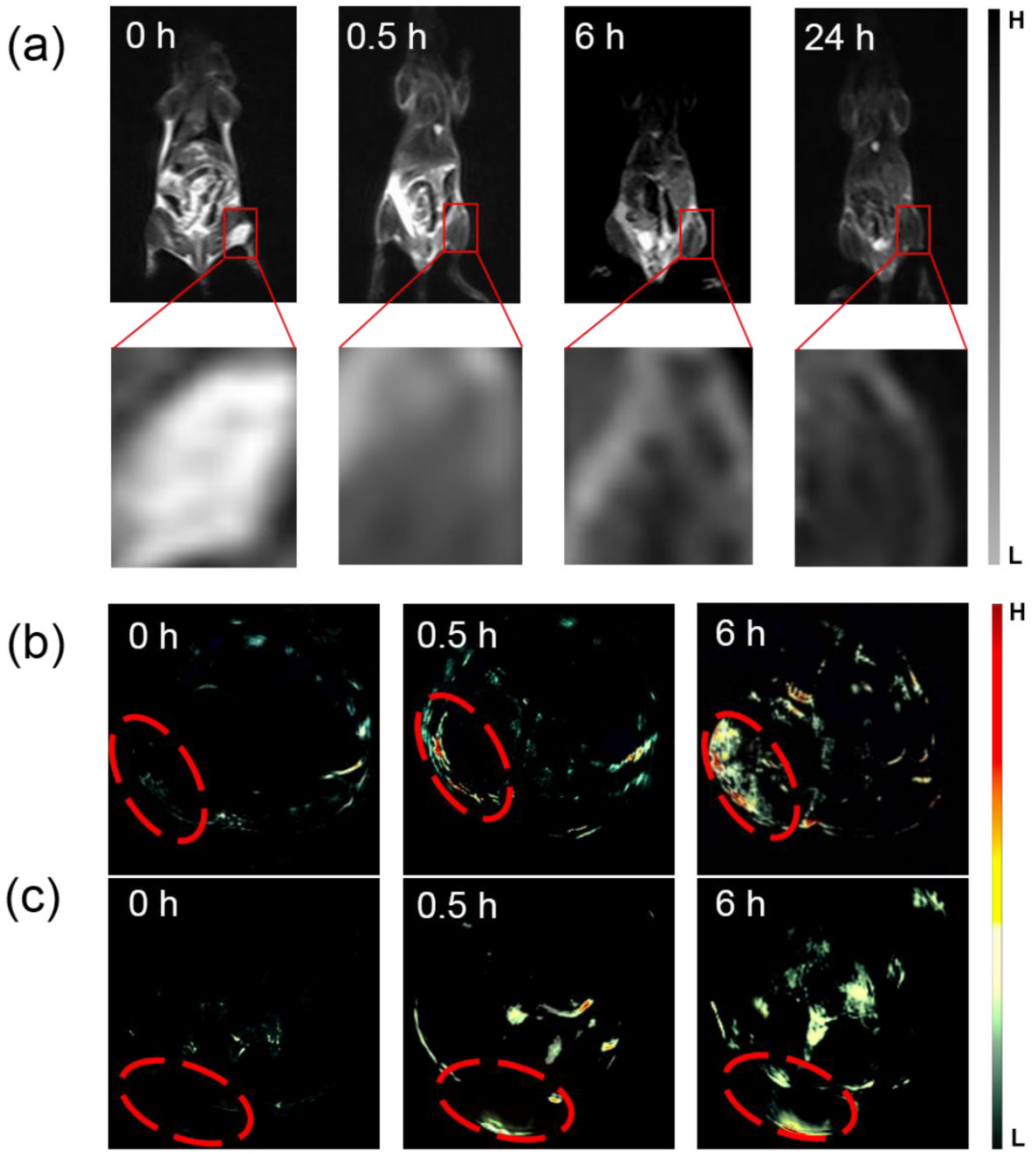

Figure 8. (a) Magnetic targeting induced *in vivo* T_2-weighted MR imaging obtained at different time intervals before and after *i.v.* injection and the amplification of the tumor sites for the enhanced MR signals corresponding to the time point. (b) Magnetic targeting induced *in vivo* PAT imaging and (c) EPR effect induced *in vivo* PAT imaging acquired at different time before and after *i.v.* injection. The tumor sites were marked with red.

Magnetic targeting induced therapeutical evaluation of MSIOs for tumor bearing mice

On the basis of the promising *in vitro* magnetic targeting PTT results, we next studied the *in vivo* photothermal therapeutic effect of the MSIOs. After the tumor sizes reached ~100 mm^3, MSIOs were injected into the tumor-bearing mice through *i.v.* injection (100 μL, 1 mg/mL). The mice were divided into four groups: (I) PBS injection (n= 3); (II) PBS + NIR laser (n=3); (III) MSIOs injection + NIR laser (n=3); (IV) MSIOs + magnet targeting + NIR laser (n=3). Laser irradiation was carried out after *i.v.* injection of MSIOs for 24 h. During the whole PTT course, the tumor temperature changes *in vivo* were monitored by an IR thermal camera. In Figure 9a-b, upon the 808 nm laser irradiation at a power of 0.6 W/cm^2, the tumor temperature of the (II) group treated with PBS followed by 12 min of laser irradiation was raised by about 3.5 °C. The other parts of the body for the mice without laser irradiation appeared a negligible temperature increase. In contrast, the temperatures on the tumor areas of mice from MSIOs + magnet targeting + NIR laser (IV) group rapidly increased to 47 °C (ΔT = 22°C), which was high enough to ablate tumors *in vivo*. However, for the PTT from the MSIOs + NIR laser group (III), the temperature can only increase to 42°C (ΔT = 17 °C) (Figure 9b). The tumor sizes were measured by a caliper every other day after the treatments. As shown in Figure 9c, the tumor volume changes of the mice treated in different groups as a function of time were recorded. It can be seen that the

tumor volumes and tumor growth rates (Supplementary Figure S11b) in group (I) and (II) showed negligible difference, suggesting that the 808 nm NIR laser irradiation did not affect the tumor growth. In contrast, the tumors in group (III) decrease obviously, indicating the EPR effect of the MSIOs under 808-nm NIR laser irradiation also take some effect on the tumor inhibition. Most importantly, the tumors in group (IV) handled with magnetic targeting + MSIOs + NIR laser showed slight scars after 2 days and gradually disappeared after 9 days for all the mice (Figure 9c), only leaving black scars at the original sites without recurrence within 15 day as shown in the comparison of the tumor photos before (0 day) and after treatment (15 day) in Figure 9e. Moreover, the tumor weights and the tumor photos for the four groups after treatments for 15 day were shown in Figure 9d and 9f, respectively, further indicating that the tumor of group (IV) with magnetic targeting + NIR laser had good treatment effect to the tumor compared with the effect of group (III). All these results further indicate that the low dose of MSIOs theranostic agent had a significantly enhanced tumor magnetic targeting ability under the external magnet for effective PTT therapy and greatly inhibit tumor growth *in vivo*.

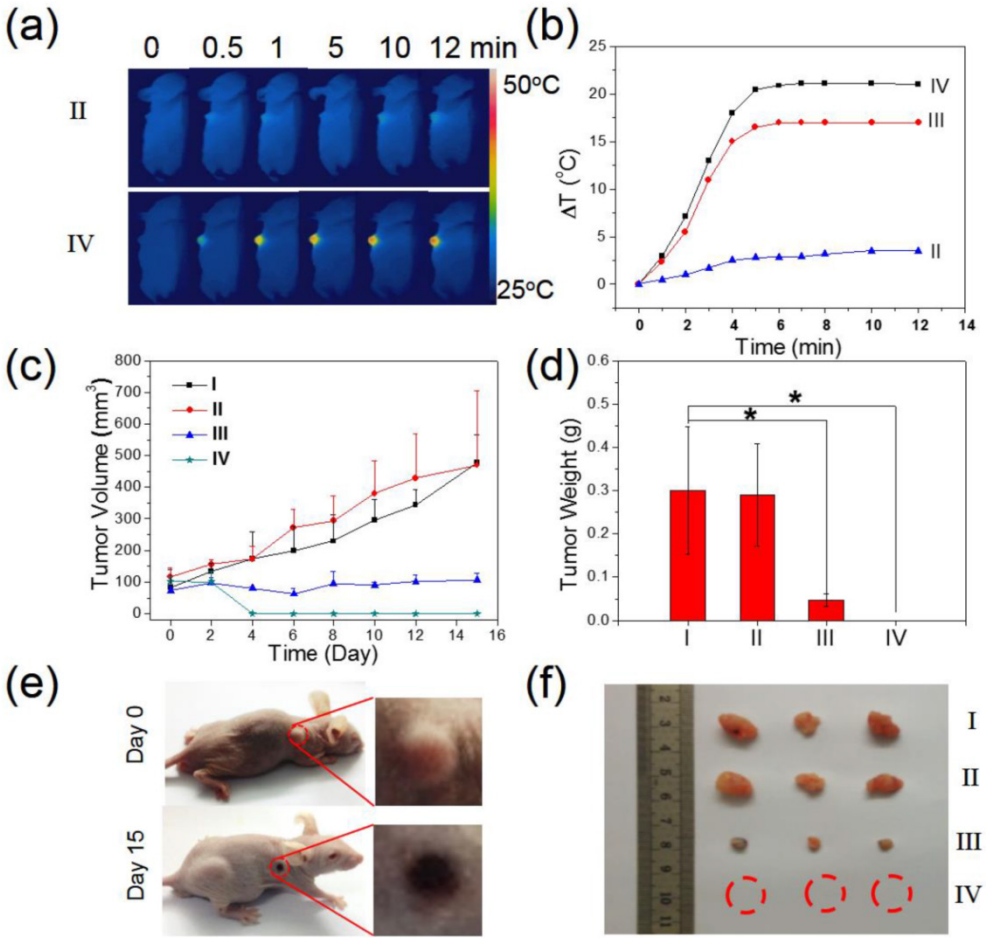

Figure 9. *In vivo* magnetic targeting-enhanced cancer therapy. Four groups of tumor-bearing mice with subcutaneous tumors were used: (I) PBS injection, (II) PBS + NIR laser exposure, (III) MSIOs + NIR laser, and (IV) MSIOs + magnetic targeting + NIR laser. (a) Typical full-body NIR thermal images of two tumor-bearing mice injected with PBS (group II) and the MSIOs *via i.v.* injection under the magnetic targeting (group IV), respectively, irradiated by 808 nm laser at different time points. (b) Temperature change of the group II and group IV. (c) Tumor growth curves of the four groups in the period of 15 day and (d) tumor weights after the treatment of 15 day. P values: *$p < 0.05$. (e) Representative photos of the group (IV) before (0 day) and after treatment (15 day). The magnified photo shows the tumor leaving black scar after the treatment. (f) Representative photos of tumors in the four groups after treatment of 15 days, suggesting an effective treatment for the magnet targeting PTT *in vivo*.

4. Conclusion

In summary, multifunctional PEG-modified superparamagnetic MoS_2/Fe_3O_4 (MSIOs) nanocomposite with good biocompatibility in physiological environment has been successfully prepared via a simple two-step hydrothermal route. Accordingly, it is demonstrated that the MSIOs is firstly used as a novel theranostic agent for *in vivo* dual-modal T_2-weighted MR and PAT imaging. Importantly, the magnetic targeting MSIOs can more effectively ablate cancer and show an enhanced photothermal therapy inhib-

iting effect to cancer with exposure to 808 nm NIR laser, while neither the MSIOs nor the laser alone have significant influence on the cancer cells. This multifunctional MSIOs nanocomposite has a great potential for MR/PAT imaging-guided focused magnetic targeting PTT of cancer spatially/timely controlled by the external magnetic field. The construction of the smart MSIOs nanotheranostic agents will open up a new avenue in the monitoring cancer therapeutic response process and efficiently avoiding the destruction to surrounding normal tissue.

Supplementary Material

Photothermal Performance Measurements, Figures S1-S11, Table S1.
http://www.thno.org/v05p0931s1.pdf

Acknowledgements

This work was supported by National Basic Research Programs of China (973 program, No. 2012CB932504 and No. 2015CB932104), National Natural Science Foundation of China (No. 21303200, 51372206, 21177128, and 21320102003), and Doctorate Foundation of Northwestern Polytechnical University (No. CX201323).

Competing Interests

The authors report no conflicts of interest.

References

1. Shanmugam V, Selvakumar S, Yeh C-S. Near-infrared light-responsive nanomaterials in cancer therapeutics. Chem Soc Rev. 2014; 43: 6254-87.
2. Cheng L, Wang C, Ma X, Wang Q, Cheng Y, Wang H, et al. Multifunctional upconversion nanoparticles for dual-modal imaging-guided stem cell therapy under remote magnetic control. Adv Funct Mater. 2013; 23: 272-80.
3. Piao J-G, Wang L, Gao F, You Y-Z, Xiong Y, Yang L. Erythrocyte membrane is an alternative coating to polyethylene glycol for prolonging the circulation lifetime of gold nanocages for photothermal therapy. ACS Nano. 2014; 8: 10414-25.
4. Robinson JT, Tabakman SM, Liang Y, Wang H, Sanchez Casalongue H, Vinh D, et al. Ultrasmall reduced graphene oxide with high near-infrared absorbance for photothermal therapy. J Am Chem Soc. 2011; 133: 6825-31.
5. Huang P, Lin J, Li W, Rong P, Wang Z, Wang S, et al. Biodegradable gold nanovesicles with an ultrastrong plasmonic coupling effect for photoacoustic imaging and photothermal therapy. Angew Chem Int Ed. 2013; 52: 13958-64.
6. Liu H, Chen D, Li L, Liu T, Tan L, Wu X, et al. Multifunctional gold nanoshells on silica nanorattles: A platform for the combination of photothermal therapy and chemotherapy with low systemic toxicity. Angew Chem Int Ed. 2011; 50: 891-5.
7. Yue C, Liu P, Zheng M, Zhao P, Wang Y, Ma Y, et al. IR-780 dye loaded tumor targeting theranostic nanoparticles for NIR imaging and photothermal therapy. Biomaterials. 2013; 34: 6853-61.
8. Liu J, Zheng X, Yan L, Zhou L, Tian G, Yin W, et al. Bismuth sulfide nanorods as a precision nanomedicine for *in vivo* multimodal imaging-guided photothermal therapy of tumor. ACS Nano. 2015; 9: 696-707.
9. Chen Y, Chen H, Zeng D, Tian Y, Chen F, Feng J, et al. Core/shell structured hollow mesoporous nanocapsules: A potential platform for simultaneous cell imaging and anticancer drug delivery. ACS Nano. 2010; 4: 6001-13.
10. Jain PK, El-Sayed IH, El-Sayed MA. Au nanoparticles target cancer. Nano Today. 2007; 2: 18-29.
11. Black KCL, Wang Y, Luehmann HP, Cai X, Xing W, Pang B, et al. Radioactive ^{198}Au-doped nanostructures with different shapes for *in vivo* analyses of their biodistribution, tumor uptake, and intratumoral distribution. ACS Nano. 2014; 8: 4385-94.
12. Skrabalak SE, Chen J, Au L, Lu X, Li X, Xia Y. Gold nanocages for biomedical applications. Adv Mater. 2007; 19: 3177-84.
13. Chakravarty P, Marches R, Zimmerman NS, Swafford AD-E, Bajaj P, Musselman IH, et al. Thermal ablation of tumor cells with antibody-functionalized single-walled carbon nanotubes. Proc Natl Acad Sci USA. 2008; 105: 8697-702.
14. Zhou M, Zhang R, Huang M, Lu W, Song S, Melancon MP, et al. A chelator-free multifunctional [^{64}Cu]CuS nanoparticle platform for simultaneous micro-PET/CT imaging and photothermal ablation therapy. J Am Chem Soc. 2010; 132: 15351-8.
15. Chen Z, Wang Q, Wang H, Zhang L, Song G, Song L, et al. Ultrathin PEGylated $W_{18}O_{49}$ nanowires as a new 980 nm-laser-driven photothermal agent for efficient ablation of cancer cells *in vivo*. Adv Mater. 2013; 25: 2095-100.
16. Gao F-P, Lin Y-X, Li L-L, Liu Y, Mayerhöffer U, Spenst P, et al. Supramolecular adducts of squaraine and protein for noninvasive tumor imaging and photothermal therapy *in vivo*. Biomaterials. 2014; 35: 1004-14.
17. Yu J, Yang C, Li J, Ding Y, Zhang L, Yousaf MZ, et al. Multifunctional Fe_5C_2 nanoparticles: A targeted theranostic platform for magnetic resonance imaging and photoacoustic tomography-guided photothermal therapy. Adv Mater. 2014; 26: 4114-20.
18. Peng J, Qi T, Liao J, Chu B, Yang Q, Qu Y, et al. Mesoporous Magnetic Gold "Nanoclusters" as Theranostic carrier for chemo-photothermal co-therapy of breast cancer. Theranostics. 2014; 4: 678-92.
19. Yin W, Yan L, Yu J, Tian G, Zhou L, Zheng X, et al. High-throughput synthesis of single-layer MoS_2 nanosheets as a near-infrared photothermal-triggered drug delivery for effective cancer therapy. ACS Nano. 2014; 8: 6922-33.
20. Chou SS, Kaehr B, Kim J, Foley BM, De M, Hopkins PE, et al. Chemically exfoliated MoS_2 as near-infrared photothermal agents. Angew Chem Int Ed. 2013; 52: 4160-4.
21. Liu T, Wang C, Gu X, Gong H, Cheng L, Shi X, et al. Drug delivery with pegylated MoS_2 nano-sheets for combined photothermal and chemotherapy of cancer. Adv Mater. 2014; 26: 3433-40.
22. Liu T, Shi S, Liang C, Shen S, Cheng L, Wang C, et al. Iron oxide decorated MoS_2 nanosheets with double PEGylation for chelator-free radiolabeling and multimodal imaging guided photothermal therapy. ACS Nano. 2015; 9: 950-60.
23. Shi Y, Huang JK, Jin L, Hsu YT, Yu SF, Li LJ, et al. Selective decoration of Au nanoparticles on monolayer MoS_2 single crystals. Sci Rep. 2013; 3: 1839.
24. Liu Y-T, Duan Z-Q, Xie X-M, Ye X-Y. A universal strategy for the hierarchical assembly of functional 0/2D nanohybrids. Chem Commun. 2013; 49: 1642-4.
25. Choi H, Choi SR, Zhou R, Kung HF, Chen IW. Iron oxide nanoparticles as magnetic resonance contrast agent for tumor imaging via folate receptor-targeted delivery. Acad Radiol. 2004; 11: 996-1004.
26. Montet X, Weissleder R, Josephson L. Imaging pancreatic cancer with a peptide−nanoparticle conjugate targeted to normal pancreas. Bioconjugate Chem. 2006; 17: 905-11.
27. Gu FX, Karnik R, Wang AZ, Alexis F, Levy-Nissenbaum E, Hong S, et al. Targeted nanoparticles for cancer therapy. Nano Today. 2007; 2: 14-21.
28. Hu J, Zhu X, Li H, Zhao Z, Chi X, Huang G, et al. Theranostic Au cubic nano-aggregates as potential photoacoustic contrast and photothermal therapeutic agents. Theranostics. 2014; 4: 534-45.
29. Huang P, Li Z, Lin J, Yang D, Gao G, Xu C, et al. Photosensitizer-conjugated magnetic nanoparticles for *in vivo* simultaneous magnetofluorescent imaging and targeting therapy. Biomaterials. 2011; 32: 3447-58.
30. Dong W, Li Y, Niu D, Ma Z, Gu J, Chen Y, et al. Facile synthesis of monodisperse superparamagnetic Fe_3O_4 core@hybrid@Au shell nanocomposite for bimodal imaging and photothermal therapy. Adv Mater. 2011; 23: 5392-7.
31. Chen Y, Guo F, Qiu Y, Hu H, Kulaots I, Walsh E, et al. Encapsulation of particle ensembles in graphene nanosacks as a new route to multifunctional materials. ACS Nano. 2013; 7: 3744-53.
32. Chen Y, Chen H, Zhang S, Chen F, Zhang L, Zhang J, et al. Multifunctional mesoporous nanoellipsoids for biological bimodal imaging and magnetically targeted delivery of anticancer drugs. Adv Funct Mater. 2011; 21: 270-8.
33. Lin L-S, Cong Z-X, Cao J-B, Ke K-M, Peng Q-L, Gao J, et al. Multifunctional Fe_3O_4@polydopamine core–shell nanocomposites for intracellular mRNA detection and imaging-guided photothermal therapy. ACS Nano. 2014; 8: 3876-83.
34. Song X, Gong H, Yin S, Cheng L, Wang C, Li Z, et al. Ultra-small iron oxide doped polypyrrole nanoparticles for *in vivo* multimodal imaging guided photothermal therapy. Adv Funct Mater. 2014; 24: 1194-201.
35. Hwang H, Kim H, Cho J. MoS_2 nanoplates consisting of disordered graphene-like layers for high rate lithium battery anode materials. Nano Lett. 2011; 11: 4826-30.
36. Wan J, Tang G, Qian Y. Room temperature synthesis of single-crystal Fe_3O_4 nanoparticles with superparamagnetic property. Appl Phys A-mater. 2007; 86: 261-4.
37. Ramakrishna Matte HSS, Gomathi A, Manna AK, Late DJ, Datta R, Pati SK, et al. MoS_2 and WS_2 analogues of graphene. Angew Chem Int Ed. 2010; 49: 4059-62.
38. Li H, Zhang Q, Yap CCR, Tay BK, Edwin THT, Olivier A, et al. From bulk to monolayer MoS_2: Evolution of raman scattering. Adv Funct Mater. 2012; 22: 1385-90.
39. Liu Y, Yu Y-X, Zhang W-D. MoS_2/CdS heterojunction with high photoelectrochemical activity for H_2 evolution under visible light: The role of MoS_2. J Phys Chem C 2013; 117: 12949-57.
40. Han W, Gao M. Investigations on iron sulfide nanosheets prepared via a single-source precursor approach. Cryst Growth Des 2008; 8: 1023-30.

41. Grosvenor AP, Kobe BA, Biesinger MC, McIntyre NS. Investigation of multiplet splitting of Fe 2p XPS spectra and bonding in iron compounds. Surf Interface Anal. 2004; 36: 1564-74.
42. Klinbumrung A, Thongtem T, Thongtem S. Characterization and gas sensing properties of CuO synthesized by DC directly applying voltage. Appl Surf Sci. 2014; 313: 640-6.
43. Bhattarai N, Ramay HR, Gunn J, Matsen FA, Zhang M. PEG-grafted chitosan as an injectable thermosensitive hydrogel for sustained protein release. J Control Release. 2005; 103: 609-24.
44. Kamran S, Asadi M, Absalan G. Adsorption of folic acid, riboflavin, and ascorbic acid from aqueous samples by Fe_3O_4 magnetic nanoparticles using ionic liquid as modifier. Anal Methods. 2014; 6: 798-806.
45. Masoomi-Godarzi S, Khodadadi AA, Vesali-Naseh M, Mortazavi Y. Highly stable and selective non-enzymatic glucose biosensor using carbon nanotubes decorated by Fe_3O_4 nanoparticles. J Electrochem Soc. 2014; 161: B19-B25.
46. Ju Q, Tu D, Liu Y, Li R, Zhu H, Chen J, et al. Amine-functionalized lanthanide-doped $KGdF_4$ nanocrystals as potential optical/magnetic multimodal bioprobes. J Am Chem Soc. 2011; 134: 1323-30.
47. Li J, Hu Y, Yang J, Wei P, Sun W, Shen M, et al. Hyaluronic acid-modified Fe_3O_4@Au core/shell nanostars for multimodal imaging and photothermal therapy of tumors. Biomaterials. 2015; 38: 10-21.